RESEARCH ARTICLE

Processing of mobile laser scanning data for large-scale deformation monitoring of anchored retaining structures along highways

Slaven Kalenjuk[1] | **Werner Lienhart**[1] | **Matthias J. Rebhan**[2]

[1] Institute of Engineering Geodesy and Measurement Systems, Graz University of Technology, Austria

[2] Institute of Soil Mechanics, Foundation Engineering and Computational Geotechnics, Graz University of Technology, Austria

Correspondence
Slaven Kalenjuk, Graz University of Technology, Steyrergasse 30, 8010 Graz, Austria.
Email: slaven.kalenjuk@tugraz.at

Abstract

In times of steadily increasing traffic loads and extreme weather phenomena, the safe maintenance of infrastructure poses a difficult challenge to operators, especially when a vast number of aged structures exists and fundamental data is missing. This paper addresses the demand for cost-efficient deformation monitoring of anchored retaining structures along public roads. The principal idea is to process laser scans of a motor-vehicle-based mobile mapping system with a high degree of automation. Starting with scene interpretation, our processing pipeline extracts the retaining wall from the rest of the point cloud, segments the anchored elements, and computes their deformations. This method requires, however, correcting for positioning errors to obtain accurate results. We exploit the high data redundancy of road patches and line markings for alignment. Due to the high degree of automation, computations scale to large numbers of point clouds and run in a repeatable manner. Even when traveling along highways with up to 100 km/h, we achieve repeatable accuracies for tilting and lateral displacements that compare to traditional, labor-intense surveying methods.

1 | INTRODUCTION

Anchored retaining walls can withstand high lateral pressures despite their slim design. They typically stabilize deep excavations, cuts, or steep slopes where space limitation is an issue. Therefore, these structures prove especially suitable for establishing road and railway networks in mountainous regions. Since retaining walls may experience extreme loads and environmental influences, it is of social-economic importance to monitor their structural stability throughout the operational lifetime. Route availability and public safety depend on their performance.

Legal standards, such as the Eurocode 7 (E. 1997-1, 2004, section 9.7), provide numerical serviceability and ultimate limit state values for settlements and relative rotations

(tilting) for retaining walls. The herein used analytical models assume simple structural systems with primitive geometric shapes and homogenous soil strata (see Figure 1). Albeit oversimplified, it can provide a rule of thumb for real-world applications, though. More sophisticated numerical methods are capable of modeling the structural behavior better, but they typically require very detailed information on the entire system (construction and underground). Characteristic parameters of concrete structures are reinforcement distribution, concrete class, and quality. Other methods (e.g., Rebhan, Marte, Vorwagner, Tschuchnigg, & Kwapisz, 2019) account for reinforcement corrosion (Figure 1 left), tension stiffening of concrete, as well as cracking energy when estimating bearing capacity and deformation response. The loading
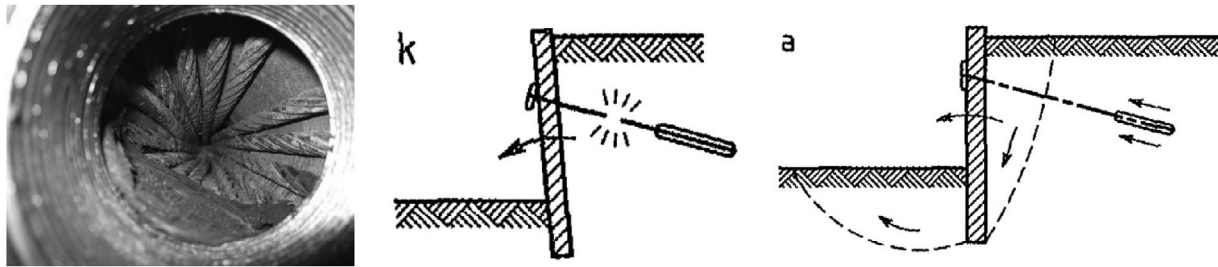
FIGURE 1 Typical failure mechanisms of anchored structures include anchor failures (center, E. 1997-1, 2004, figure 9.5) as a consequence of, for example, corroded anchor strands (left) and loss of overall stability (right, E. 1997-1, 2004, figure 9.6)
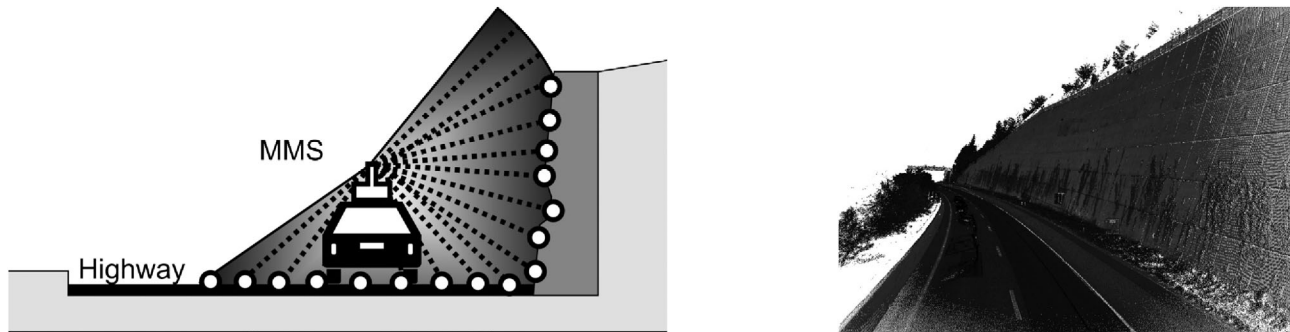

FIGURE 2 Concept for large-scale deformation monitoring of retaining walls: fast data acquisition with mobile mapping (left), producing high dense point clouds (right) for efficient and automatic data processing

behavior of the underground is at least equally important for a precise estimate. The strata, the constitutive model, and its soil parameters are influencing factors in this context (Sharma, Prabhu, Naveen, & Bhuvaneshwari, 2020).

Despite the remarkable progress, practitioners rarely profit from these models, as fundamental data are missing for most existing structures. Moreover, because of limitations in personnel and financial resources, only a fraction of infrastructure objects undergoes ongoing monitoring schemes with reasonably high measurement frequency.

In other words, infrastructure operators mostly know little about (a) the nominal and (b) the actual deformation behavior of their objects. This paper addresses the latter problem in particular. The motivation is that observations at regular intervals can help to identify abnormal structural behavior.

Established measurement methods such as optical surveys and permanently installed sensors are infeasible for this purpose because of their time and cost inefficiency. We hence propose a novel tilt monitoring concept using mobile laser scanning (MLS). The principle idea is that a mobile mapping system (MMS) scans retaining walls while passing by with up to 100 km/h (60 mp/h), that is, without constraining road availability (see Figure 2, left). The efficient data collection allows us to minimize the data acquisition costs with an increasing number of struc-

tures. Therefore, our approach promises improvements in structural monitoring at large scale, that is, when a large amount of structures exist in small space (as, for instance, in the central European area).

To the best of the authors' knowledge, the literature lacks research on processing mobile laser scans for deformation monitoring. Recent studies focus on inventory, modeling, or inspection of infrastructure objects. The present paper provides a contribution to

- processing large-scale data of commercially available MMS,
- for deformation monitoring of anchored structures and retaining walls,
- by tailored, object-oriented point cloud processing algorithms, which can model deformations of anchored concrete panels automatically,
- while accounting for the system's positioning uncertainties.

The next section gives a review of existing work about monitoring of retaining structures, static laser scanning-based deformation monitoring, and recent case studies on MLS. A detailed description of our method for highly automated point cloud processing follows in Section 3. We describe the scope conditions of the extensive case study

with multiple retaining walls in the Alpine area (Section 4) and discuss the achieved results (Section 5).

2 | RELATED WORK

2.1 | Monitoring of retaining structures

Maintaining retaining structures requires experts to inspect their stability and general condition. Elementary, but essential measures are visual inspections that take place at regular intervals. The aim is to identify and report deficiencies as well as to track their evolution. In case that problems or changes in behavior become evident, installing additional sensors helps to trace and understand the structural performance (deflections, pressures) from that point on in more detail.

For this purpose, various published use cases show that monitoring schemes typically amount to the same selection of sensor types. Yoo and Lee (2003) used total stations, inclinometers, earth pressure cells, and strain gauges along anchor rods during the construction of an anchored segmental retaining wall. This comprehensive monitoring program contributed to the fundamental understanding of the mechanical behavior of such object types. Rebhan, Marte, Tschuchnigg, Vorwagner, and Kwapisz (2019) apply strain and tilt sensors on the front face of a cantilever wall model while artificially inducing corrosion of the reinforcement at different load levels. It is their ultimate goal to quantify the extent of the corrosion, based on sensor data. Admassu, Lynch, Athanasopoulos-Zekkos, and Zekkos (2019) report on the installations of unattended, low-cost systems, with inclinometers, strain gauges, and thermometers to two existing reinforced concrete walls on highways that showed significant distress at preceding inspections.

While researchers seek for continuous and frequent data collection, recurring conventional wall surveys with total stations are sufficient and still more feasible. The reason is that reinforced concrete retaining walls tend to behave ductile, thus allowing large deformations before reaching a critical state. However, the problem of using surveying techniques and permanently installed sensors on a wall is that, although accurate, information is available only in single points/profiles and at a high cost. On that account, unsurprisingly, imaging systems provide cheap alternatives for full-field analysis. Tung, Weng, and Shih (2013) use a standard camera with a fixed setup to repeatedly capture images of a retaining wall and to perform digital image correlation. This method is sensitive to in-plane deformations only and comprises the challenge of setup stability for pure imaging systems (Ehrhart, 2017). Standard photogrammetry proves adequate neither, since

3D reconstructions do not yield the desired accuracy for deformation monitoring (Oats, Escobar-Wolf, & Oommen, 2017), except when observing visual markers (S. Park, Park, Kim, & Adeli, 2015). In contrast, laser scanning established itself as a precise alternative for full-field data acquisition. Back in 2008, Laefer and Lennon (2008) concluded that this technology was not ready for their task of automated monitoring of sheet pile walls. The main reasons were the high equipment costs and the lack of software tools for change detection in point clouds. Powered by the rapidly growing market, applications of laser scanning for civil engineering increased in the past years with cheaper hardware options and smarter software solutions. Among other fields, research in civil engineering capitalizes on these recent developments. Oskouie, Becerik-Gerber, and Soibelman (2016) show promising results of a field study where they target settlements of a mechanically stabilized earth (MSE) wall with laser scanning. Their concept for data processing is to extract horizontal joints between the concrete panels and to compare their height component with data of subsequent epochs. By contrast, McGuire, Yust, and Collin (2016) obtain vertical profiles from point clouds of full-scale structures, from which they compute vertical and lateral displacements. Another recent field study focuses on the out-of-plane offsets between adjacent concrete facing panels of a scanned MSE wall (Lin, Habib, Bullock, & Prezzi, 2019). These investigations reveal the potential of terrestrial laser scanning when using appropriate hardware and tailored processing strategies. Results differ from manual measurements less than 1–2 mm at spot checks.

2.2 | Processing strategies for laser scanning-based deformation monitoring

Laser scanning is a promising technology for deformation monitoring that can produce remarkable results. Its accuracy depends on a variety of influencing factors though. Regarding laser distance measurements, these subdivide into three main categories of influences, all of which are subject to current research (Lienhart, 2017; Blaskow & Schneider, 2014). These include impacts of

1. instrument hardware and setup stability,
2. measurement path, and
3. interaction of laser beam with target.

Accordingly, obtaining maximum accuracy requires considerations about (a) instrument calibration (Holst, Neuner, Wieser, Wunderlich, & Kuhlmann, 2016) and reliable registration (Cheng et al., 2018; Friedli & Wieser, 2016), (b) refractivity and atmospheric corrections

(Friedli, Presl, & Wieser, 2019), as well as (c) the noise level as a function of surface characteristics and incidence angles (Soudarissanane, Lindenbergh, Menenti, & Teunissen, 2011; Wujanz, Burger, Mettenleiter, & Neitzel, 2017).

Apart from these aspects, the question remains of how to quantify deformations from multiple point clouds in general. Compared to traditional surveys of optical targets, laser scanners capture surrounding objects fast and autonomously, with no guarantee of sampling the same spot multiple times. Obviously, the challenge is to find corresponding points in both point clouds to compare their coordinates (*X*, *Y*, *Z*). Standard software packages for point cloud processing (e.g., CloudCompare) include algorithms that search for nearest neighbors (Girardeau-Montaut, Roux, Marc, & Thibault, 2005) or points with the least orthogonal distance w.r.t. the underlying surface (Lague, Brodu, & Leroux, 2013). These methods work well for most cases but prove prone to varying point densities, registration errors, and in-plane movements (Holst, Schmitz, Schraven, & Kuhlmann, 2017). Finding the correct, corresponding points is the key here, similar to tasks of point cloud registration, object reconstruction, and tracking. Research on these topics produced various algorithms that compute hand-crafted geometric features for two point clouds and find the nearest neighbor in feature space (Guo et al., 2016). Today, state-of-the-art descriptors rely on training deep networks with freely available data sets that outperform hand-crafted ones in terms of accuracy (Choy, Park, & Koltun, 2019). This fact is especially beneficial for deriving deformations of irregular objects, such as landslides (Gojcic, Zhou, & Wieser, 2019).

However, most artificial structures consist of regular shapes, providing less distinctive points in the laser scans. Gordon and Lichti (2007) exploit just this smoothness property by modeling point clouds of timber beams. Through the high data redundancy, they achieve a precision of beam deflection that is up to 20 times better than the instrument's single-point precision. This concept applies to objects of diverse shapes, ranging from arch dams (Eling, 2009), bridges (H. S. Park, Lee, Adeli, & Lee, 2007), tall chimneys (Kregar, Ambrožiĉ, Kogoj, Vezoĉnik, & Marjetiĉ, 2015), radio telescopes (Holst et al., 2015), and igloos (Serantoni & Wieser, 2016) to other special constructions with free-form surfaces (Schmitt et al., 2017).

Mukupa, Roberts, Hancock, and Al-Manasir (2017) and Vosselman and Maas (2010) review various field studies and highlight the variety of tailored, problem-specific solutions to processing static, terrestrial laser scans for deformation monitoring.

2.3 | Mobile laser scanning in civil engineering

While static laser scanning established itself in engineering applications, the commercialization of MLS systems is underway (Tapken, 2018). It is their ability to collect extensive data of road environments that makes MLS an appealing technology for infrastructure modeling and inventory (Jaakkola, Hyyppä, Hyyppä, & Kukko, 2008; Ma et al., 2018) as well as for generating accurate maps for autonomous driving (Javanmardi, Javanmardi, Gu, & Kamijo, 2018; Ladstädter, Luley, Ladstätter, & Mayer, 2019). Improvements in profile scanners and positioning sensors push the quality of MLS data further. Albeit originally introduced for mapping, state-of-the-art systems provide useful data for as-is state analysis of road infrastructure. Especially road surface inspections on, for example, ruts, cracks, and potholes gained attention in research (Heinz, Eling, Klingbeil, & Kuhlmann, 2019) and industry (Saarenketo & Silvast, 2019). The reason is that reliable information about the location and the extent of existing deficiencies allows competent operators to perform tailored rehabilitation measures without constraining road availability during an inspection. MLS produces large amounts of data within a short time, making manual identification of regions of interest unfeasible with increasing project size. Automated pattern recognition algorithms are therefore in high demand for processing laser scans of road surfaces (Sesselmann, Stricker, & Eisenbach, 2019) and, for instance, of tunnel linings (Schneider, Prokopová, Modetta, & Petschen, 2019).

With a focus on defect detection and clearance measurements (Mikrut et al., 2016), MLS found its way to civil engineering tasks. Up to date, few works exist on deformation monitoring using MLS data, though. This is mainly due to missing algorithms that derive deformations (see Section 2.2) and handle registration errors of MLS point clouds in a scalable, efficient, and automatic manner.

3 | METHODOLOGY

This section describes such algorithms that take a point cloud *P* (Figure 4, left) from an MMS and compute deformations for retaining walls. It assumes *P* to sample road sections with the object of interest and its surroundings. The methodology exploits the fact that most commercial MLS systems enable data partitioning during acquisition. This feature reduces the processing time of trajectories and georeferenced point clouds. Uncropped laser scans of large-road networks would require an additional action before proceeding with the proposed processing pipeline.
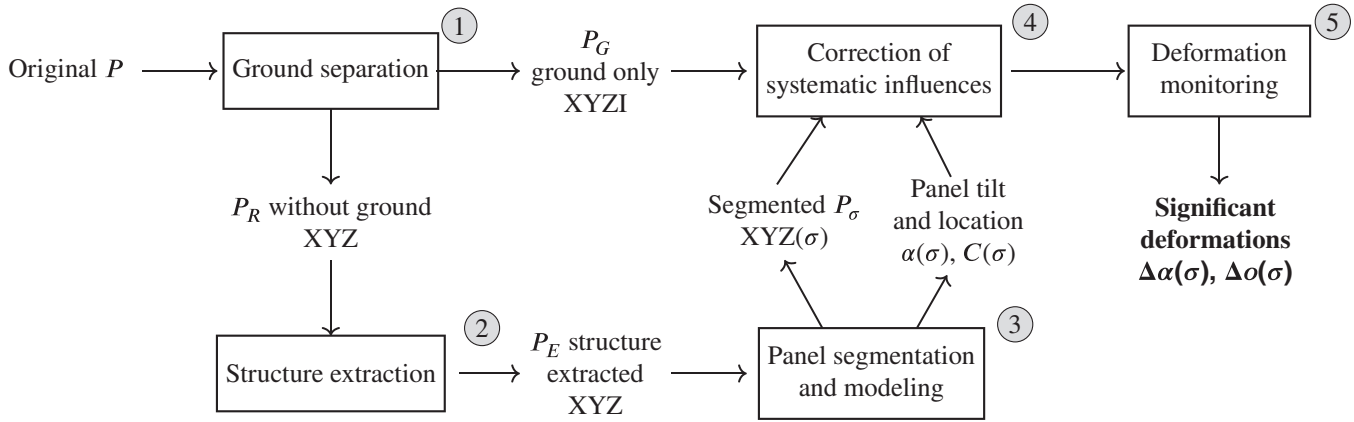
FIGURE 3 Proposed workflow for point-cloud-based deformation monitoring of retaining walls

It is depicted in Figure 3 and consists of five computational steps:

1. *Removing ground points* implies the positive effect of accelerating all subsequent computations. Moreover, the separated ground cloud P_g allows road-specific analyses.

2. A binary classification follows that *extracts the retaining wall* from the remaining point cloud and thus removes vegetation, cars, street signs, etc.

3. As reviewed in Section 2.2, modeling point clouds of regularly shaped objects and their deformations is preferable to computing point-to-point deviations. The idea is hence to *segment anchored concrete panels* and *model* them individually with planar surfaces.

4. Positioning uncertainties and calibration insufficiencies of MMS are limiting factors when it comes to accurately monitoring deformations. Even existing coregistration methods fail to *fix these systematic influences* in the hundredths of a degree accuracy range. Our proposed solution does better by relying on the stability of the road surfaces.

5. The final step of the processing pipeline *computes deformations* and tests them for significance.

3.1 | Ground separation

Most high-end MLS systems have two profile laser scanners arranged in butterfly configuration, producing a cross-pattern-sampling of the pavement with high resolution. Indeed, MLS generates point clouds with up to two-thirds of all points lying on the road surface or ground. Therefore, it is not surprising that most processing strategies start with extracting these points, whether for detailed pavement analysis or infrastructure inventory (Ma et al., 2018). The herein described method aims to reduce the data amount and to accelerate processing time by doing so.

Given the set P of points $P_{i_P} \longleftarrow \vec{p} = [p_x, p_y, p_z, p_{int}]^T$, we construct a discretized three-dimensional grid G around the sampled scene. Each grid cell defines the bounding box for a subset $P' \subset P$ by its centroid coordinates $G(i, j, k) \longleftarrow \vec{g} = [g_x, g_y, g_z]$ and its predefined size s

$$P' = f(G(i, j, k), P, s). \tag{1}$$

Unlike in voxel representations, our grid spacing is nonuniform, that is, it differs in vertical and
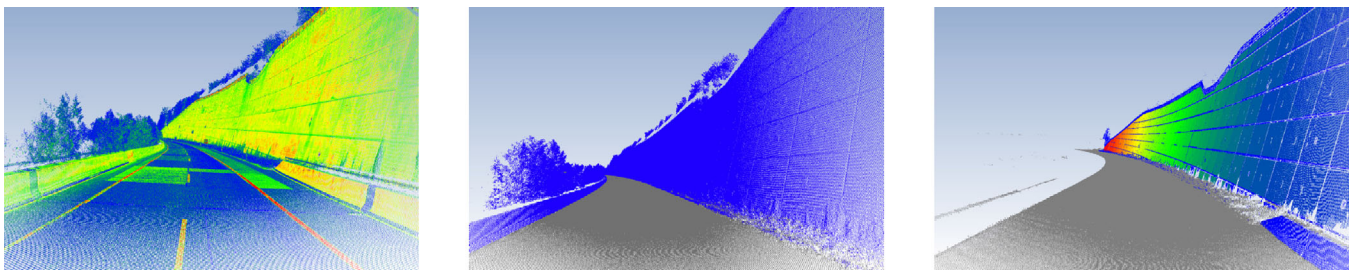

FIGURE 4 Raw intensity point cloud (left), point subsets after ground classification (middle) and after concrete panel segmentation (right)

horizontal direction $s_x = s_y \neq s_z$ in general. The domain of the indices i, j, k depends on the dimensions of the sampled scene.

The underlying idea of our processing strategy is a seeded cell-based region growing. It exploits two main characteristics of the sampled ground or road surface: (a) its point density and (b) its horizontality. While the former property results from data acquisition with MMS, the latter implies that the ground is the object with the least height variation per distance. Noteworthy, this assumption holds for inclined roads as well.

To find a potential seed cell, we start by searching for the vertical slice of grid cells with the maximum point number

$$k_{\max} = \operatorname*{argmax}_k \sum_j \sum_i |P'|, \tag{2}$$

where P results from (1) and $| \cdot |$ denotes the cardinality of the point set. Prerequisite is the appropriate choice of the cell height s_z so that the histogram can capture the predominance of the ground points in the scene representatively.

Within all cells of this extracted grid slice $G_{i,j,k_{\max}}$, we look for the one that maximizes the point number while minimizing the z-variation

$$i_{\max}, j_{\max} = \operatorname*{argmax}_{i,j} \frac{|P'|}{\sigma(Z')} \qquad \text{with}$$
$$Z' = \left\{ z'_{i_P} \longleftarrow p_z \in P'_{i_P} \right\}. \tag{3}$$

The region growing procedure starts at the found seed cell. Its region grows with neighboring cells in case that their minimum z-values do not differ more than a predefined threshold δ_z. The criterion should be multiple times greater than the noise of the laser scans on the ground.

Accumulation of all points within the grown cells yields the cloud with ground points P_G (gray point cloud in Figure 4, middle) and the one without $P_R = P \setminus P_G$ (blue cloud).

3.2 | Extraction of the retaining wall

Within the remaining data set P_R, the sampled retaining wall is presumably smooth and tall. Such properties are in marked contrast to vehicles, road signs, or vegetation, resulting in their removal when implementing this logic. Well-established indicators for a point cloud's smooth or roughness are surface normals $\vec{n}$ and their associated

---

Algorithm 1 Ground separation

1: **function** FINDSEEDCELL P, s_x, s_y, s_z
2:   **in**: P, s_x, s_y, s_z
3:   Generate grid $G_{i,j,k} \leftarrow \vec{g} = [g_x, g_y, g_z]^T$
4:   **for** each vertical layer k in grid **do**
5:     **for** each grid cell i, j in layer k **do**
6:       extract $P' \in P$ in grid cell using f (1)
7:       count point number in cells $n \leftarrow n + |P'|$
8:     **end for**
9:     $N_k \leftarrow n, n \leftarrow 0$
10:   **end for**
11:   find layer with max. point number $k_{max} = \operatorname*{argmax}_k N_k$
12:   **for** each grid point $G_{i,j,k_{max}}$ **do**
13:     extract points in grid P'
14:     generate set Z' of z coordinates using (3)
15:     compute metric $\mu_{i,j} = |P'|/\sigma(Z')$
16:   **end for**
17:   find seed cell in layer k that maximizes
       $i_{max}, j_{max} = \operatorname*{argmax}_{i,j} \mu_{i,j}$
18: **return** $i_{max}, j_{max}, k_{max}$
19: **end function**

1: **function** REGIONGROWING $\vec{g}_s \longleftarrow G_{i_{max},j_{max},k_{max}}$
2:   **in**: $\vec{g}_s \longleftarrow G_{i_{max},j_{max},k_{max}}$
3:   initialize region growing candidates $C \longleftarrow \{\vec{g}\}$
4:   initialize list of available grid points $A \longleftarrow \{\vec{g}\}$
5:   **while** $C \neq \emptyset$ **do**
6:     $\vec{c} \leftarrow C_1$
7:     $C \leftarrow C \setminus C_1$
8:     extract $P'_c \in P$ in grid cell with f using (1)
9:     find grid neighbors for $\vec{c}$ in A: $N = \Omega(\vec{c}, A, 1)$
10:    **for** $\vec{n} \in N$ **do**
11:      extract $P'_c, P'_n, \in P$ in grid cell f (1)
12:      generate set Z'_c, Z'_n of z coordinates using (3)
13:      **If** $|\min Z'_c - \min Z'_n| \leq \delta_z$ **then**
14:        $C \leftarrow C \cup \{\vec{n}\}$
15:        $A \leftarrow A \setminus \{\vec{n}\}$
16:        $P_G \leftarrow P_G \cup P'_n$
17:      **end if**
18:    **end for**
19: **end while**
20: **end function**

surface variations σ (Pauly, Gross, & Kobbelt, 2002). These values derive from principal component analysis (PCA) on the covariance matrix (or local structure tensor) Σ of the local neighborhood N around each point p in the cloud

$$\Sigma = \frac{1}{n} \sum_{i=1}^{n} \left(\nu_i - \overline{N} \right) \left(\nu_i - \overline{N} \right)^T$$

$$N = \left\{ P_R \left| \|p_R - p_{R_i}\| \leq r, \; i = 1, \dots |P_R| \right. \right\}$$

and its eigenvalue decomposition $\Sigma = S \Lambda S^T$. The eigenvector $\vec{s_2}$ with $S = [\vec{s_0}, \vec{s_1}, \vec{s_2}]$ with the least eigenvalue $\lambda_0 \geq \lambda_1 \geq \lambda_2 \geq 0$ corresponds to the modeled plane normal $\vec{n}$, where the surface variation defines to $\sigma = \lambda_2/(\lambda_0 + \lambda_1 + \lambda_2)$.

Ioannou, Taati, Harrap, and Greenspan (2012) extend the idea of difference of Gaussians (DoGs) in two-dimensional (2D) to difference of normals (DoNs) in 3D. They demonstrated its applicability to extract nonsmooth infrastructure inventory from point clouds. The processing pipeline adapts this algorithm to achieve the opposite—to retain smooth and disregard nonsmooth objects.

DoN describes the difference of the surface normals $\Delta \vec{n}$ with different search radii r_s and r_l (small and large)

$$\Delta \vec{n}(p_R, r_s, r_l) = \left(\vec{n}(p_R, r_s) - \vec{n}(p_R, r_l) \right)/2. \quad (5)$$

The intuition behind $\Delta \vec{n}$ is a difference vector between points on the unit sphere, but rescaled to $r = 0.5$, so that $\Delta \vec{n}$ lies within $[0, 1]$. Accordingly, $\|\Delta \vec{n}\| \geq \epsilon$ indicates surface discontinuity around p_R (considering sensor noise and rounding errors), since the plane orientations deviate when fitting to smaller and bigger point neighborhoods. This fact is beneficial to filter out all nonsmooth points by thresholding the DoN

$$P_S = \left\{ P_R \left| \|\Delta \vec{n}(p_R, r_s, r_l,)\| \leq \|\Delta \vec{n}_{th}\| \right. \right\}. \quad (6)$$

The filtered scene contains smooth but sparse point groups yet. Spatial clustering of P_S allows to group them to logical units. Proximity c_d and subset size c_S are the criteria for forming clusters. The largest one is a cleaned up subset P_S^* of the retaining wall P_S.

One problem that remains is that thresholding in (6) may remove points of interest because of rough spots on the surface of the retaining wall. A convex hull represents a convenient solution to this problem. We use the quickhull algorithm (Barber, Dobkin, & Huhdanpaa, 1996) to construct a boundary surface (i.e., the convex hull) around, which we then use to filter the initial cloud P_R after ground removal. This concept sidesteps the adverse effects of (6) and retains the full resolution in the extracted point cloud P_E.

Algorithm 2 Structure extraction with difference of normals

1: **function** DoN$P_r, r_S, r_L, \|\Delta \vec{n}_{th}\|$
2:     **for all** $p_R \in P_R$ **do**
3:         compute surface normals $\vec{n}$ and curvature σ for neighboring points within r_l, r_s radius around p_R
4:         compute DoN: $\Delta \vec{n}(p_R, r_l, r_s)$ using (5)
5:     **end for**
6:     obtain P_S by filtering P_R using (6)
7:     **return** P_S
8: **end function**

1: **function** SPATIAL CLUSTERINGP_S, c_d, c_s
2:     initialize clusters $C \longleftarrow \emptyset$
3:     initialize set of available points $A \longleftarrow \{P_S\}$
4:     **while** $A \neq \emptyset$ **do**
5:         extract a point randomly $\vec{p} \in A, A \longleftarrow A \setminus \{\vec{p}\}$
6:         find neighborhood $N = \Omega(\vec{p}, A, c_d)$
7:         **while** $N \neq \emptyset$ **do**
8:             **if** $|C_i| + |N| < c_S$ **then**
9:                 add N to current cluster $C_i \longleftarrow N$
10:                update set of available points $A \longleftarrow A \setminus N$
11:                pick point and add its neighbors to N: $\vec{p} \in N$, $N \longleftarrow N \cup \Omega(\vec{p}, A, c_S)$
12:             **end if**
13:         **end while**
14:         initialize another cluster $i \longleftarrow i + 1, C \longleftarrow C \cup \{\}$
15:     **end while**
16:     find largest cluster $P_S^* \longleftarrow \underset{i}{\arg\max}|C_i|$
17:     **return** P_S^*
18: **end function**

3.3 | Anchored panel segmentation and modeling

When it comes to the failure of individual anchors, the consequent redistribution of loads may result in inhomogeneous deformation patterns across the structure. To account for these, it is therefore desirable to detect and investigate (anchored) concrete panels individually. The detection algorithm relies on their smoothness as well as on the vertical and horizontal block joints that separate them.

As outlined in Section 3.2, surface normals are useful to reveal continuities and discontinuities of the scanned surface. Nearby points, whose surface normals point approximately in the same direction, will likely describe a smooth surface. The outcome depends on the number of neighboring points that lie within the defined search

radius r and contribute to surface normals estimation. Multiscale approaches attempt to avoid this parameter selection in segmentation tasks (Hackel, Wegner, & Schindler, 2016). While these are less prone to varying point densities and noise, a data and task-adapted radius can provide better results, though. Essentially, the support radius needs to be small enough so that block joints become visible in the surface normals.

In fact, any smooth surface is approximable with planes at a small scale. However, the drawback of small support radii is that noise or single outliers can destabilize the total least squares plane estimates (i.e., the PCA) heavily. Consequently, we seek for a robust concrete panel segmentation at normals level (Nurunnabi, Belton, & West, 2014). In such a multivariate setting, every point ν_i in the neighborhood N, whose Mahalanobis distance (MD) to the center

$$\mathrm{MD}\left(\nu_i, \overline{N}\right) = \sqrt{\left(\nu_i - \overline{N}\right)^T \Sigma_N^{-1} \left(\nu_i - \overline{N}\right)} \qquad (7)$$

exceeds the elliptical tolerance $\sqrt{\chi^2_{3,0.975}}$ (two-sided test, significance level of 5%), is a putative outlier. Unfortunately, outliers affect the mean $\overline{N}$ and the covariance matrix Σ_N, so that MD suffers masking effects. A popular, robust estimator for location N and scatter Σ is the minimum covariance determinant (MCD). It tries to find a subset N_{MCD} with h points in the query point's neighborhood N whose covariance matrix has the smallest determinant

$$\det \Sigma_{N_{MCD}} = \lambda_1 \cdot \lambda_2 \cdot \lambda_3 \overset{!}{=} \min, \qquad (8)$$

where h is a variable integer parameter that controls the trade-off between robustness and computation speed and lies in $[(n + 4)/2; n]$. Because of its low computational efficiency, we favor the faster variant DetMCD (Hubert, Debruyne, & Rousseeuw, 2018; Rousseeuw & Driessen, 1999) over the classical MCD. The subset N_{MCD} replaces N in (4) to obtain robust normals eventually. This is a crucial step for the segmentation quality, especially when surface normals define the homogeneity criteria. Starting at any query point q in P_E, regions grow with adjacent points p in case that (a) the enclosed angle of surface normals is

$$\arccos\left(\frac{\langle \vec{n}_p, \vec{n}_q \rangle}{\|\vec{n}_p\| \cdot \|\vec{n}_q\|}\right) \leq \Delta\alpha, \qquad (9)$$

(b) the orthogonal distance is $< p - q, \vec{n}_q > \leq \Delta\Omega$, and (c) the euclidean distance does not exceed $\|p - q\| \leq \Delta\epsilon$.

3.3.1 | Modeling

Each of the resulting segments σ_π with $\pi = 1, \dots \Pi$ (Π is the total number of concrete panels) contains point subsets $P_{\sigma_\pi} \in P_E$ that represent individual concrete panels (Figure 4, right). Although the structural deformation pattern can be arbitrary, these separate logical units will experience rigid-body movements in the first place. The composition of all elements' movements then provides an intuitive and realistic model of the overall structural behavior (strain, bending, and distortion). The underlying principle is similar to finite element methods but stands out in terms of modeling quality at low complexity.

The surface of retaining walls and therefore its concrete panels are planar in most cases. However, the surface quality of these elements deteriorates over time (e.g., spalling or corrosion cracking), or vegetation may cover partial areas of the surface. Consequently, the sampled point cloud of the panels can systematically deviate from a plane. To mitigate the impact on the derived deformations, it is essential to apply robust methods such as RANSAC (random sample consensus) or DetMCD (deterministic algorithm for MCD) at this stage. The robust panel location $C_\pi \longleftarrow \overline{P_{\sigma_\pi}}$ corresponds to the centroid of the outlier-free subset. Its orientation α_π refers to the estimated plane normal $\alpha = \arccos(n_z)$.

3.4 | Compensation for systematic influences

One remaining issue is the positioning uncertainty of the mobile mapping platform. We can expect location errors from differential GNSS positioning of a few centimeters in the best case. These directly influence the computed panel location.

In terms of orientation, today's high-grade IMUs achieve roll and pitch root-mean-square (RMS) errors of better than 0.01° (Applanix, 2017). While the individual sensors suit our requirements, the combination of all sensors proved to be the limiting factor in practice. The lever arm calibration parameters change over time and with varying external influences (vibrations, temperature, etc.). A recalibration of the rotation angles with high-quality, that is, in the range of hundredths/thousandths of a degree, is challenging.

Positioning uncertainties and calibration insufficiencies evoke a tilting of the horizon with direct influence on n_z, and thus, on panel orientation α_π and on location C_π. As the MMS passes by, these systematic errors will likely affect the complete, sampled scene of the retaining wall's surroundings. Therefore, there are two ways to address these systematic influences:
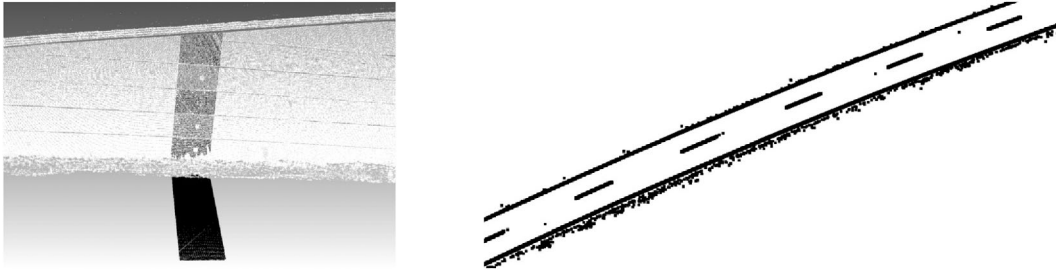
FIGURE 5 Road surface analysis for fixing systematic influences: extraction of distinct road sections by using concrete panels (left) and line markings by thresholding laser intensity (right)

1. Identifying stable areas in point clouds.
2. Estimating the systematic offset by passing by the structure in two opposite driving directions.

The former is preferable due to lower time and cost effort but applies only if the scene did not change too much, that is, no construction works took place in between the measurement campaigns.

In such road and highway settings, the road pavement is a recurring object class candidate that provides a vast number of points for alignment. However, existing point cloud registration approaches are limited when it comes to aligning road surfaces to each other. Iterative closest point (ICP) and kernel correlation (Tsin & Kanade, 2004) methods do not converge sufficiently for a large number of points and feature-based matching fails (Spezialetti, Salti, & Di Stefano, 2019; Tombari, Salti, & Di Stefano, 2013) due to the lack of key points. The problem-tailored method extracts definite, corresponding road sections $P_G(j)$ from two ground point clouds P_G (see Section 3.1). The centroid coordinates of a concrete panel, its size, and its normal vector define the cut-out region for individual columns j (see Figure 5, left). Pavements of road networks are planar surfaces in general, considering ruts and potholes to a small extent too. The robust normal vectors $\vec{n_G}(j)$ of the road sections $P_G(j)$ describe a point set on the unit sphere, typically interpreted as extended Gaussian image (EGI; Horn (1984)). This idea simplifies the registration problem and provides significant benefits in terms of

- direct correspondences between points (panel columns),
- translational invariance of the normals.

The rotation matrix that aligns the EGI $p = \vec{n_G}(j, t_2)$ and $q = \vec{n_G}(j, t_1)$ best in a least-squares sense is $\sum_{i=1}^{m} w_i |R\, p_i - q_i| \overset{!}{=}$ min. According to Sorkine (2009), R results from

$$x_i = p_i - \overline{p} \qquad y_i = q_i - \overline{q},$$

$$S = X Y^T,$$

$$S = U \Sigma V^T,$$

$$R = V \operatorname{diag}\left(1, 1, \det\left(V\, U^T\right)\right) U^T. \tag{10}$$

Through incorporating (10) in an iterative RANSAC scheme, outlier-free correspondences $X \longleftrightarrow Y$ remain for the least-squares estimation.

Recalling that P_G is a sample of a surface with small height variations, the quality varies for the estimated rotation angles $R = R_z(\phi)\, R_y(\theta)\, R_x(\psi)$. While the heading angle is less reliable, the high point density of the road sections allows fixing the horizon tilting with θ and ψ accurately.

For bias-free panel locations C, it is necessary to fix another three degrees of freedom: heading (ϕ) and translation (x, y). On that account, we extract road line markings based on the reflected laser intensity signal (see Figure 5, right) for both epochs t_1 and t_2. We establish direct correspondences through the centroids of the segmented line markings and compute a 2D variant of (10) to retrieve $R \in \mathbb{R}^2$ and $\vec{t} = [t_x, t_y]^T$. We can disregard t_z and leave one degree of freedom unresolved because

1. tilting and lateral displacements are a more common failure mode than settlements (see Section 1) and
2. laser scanners are less sensitive to in-plane movements.

3.5 | Deformation monitoring

Changes in the plane's key parameters thus indicate structural deformations between two epochs t_{n-1} and t_n. Tilting of the concrete panel $\Delta\alpha$ refers to the plane's tilt change w.r.t. the z-axis and lateral displacement Δo corresponds to the averaged orthogonal distance to the fitted plane

Algorithm 3 Compensation for systematic errors

1: **function** FIXROLLPITCH$C(t_1, t_2), N(t_1, t_2), P_G(t_1, t_2), l, w$

2:     cluster panel centroids, normals to columns C^*, N^*

3:     **for** $j \longleftarrow 1, \ldots, |C^*|$ **do**

4:       extract coordinates $\vec{p} \longleftarrow C^*_{j_c} \in C^*_j$ and surface normal $\vec{n} \longleftarrow N^*_{j_c} \in N^*_j$ of one element within column j

5:       compute 2D boundaries for road surface $B_{i,k} = \vec{p} + \delta_{i,k} \cdot \vec{n} \cdot l \pm \vec{q} \cdot w$ with $\exists \vec{q} [|\vec{p}| \cdot |\vec{q}| = 0]$ and $i, k = [0, 1]$

6:       extract road surface patch $P_G(j)$ with B

7:       compute road normal $\vec{n}_G(j)$

8:     **end for**

9:     compute rotation matrix R using (10)

10:    **return** R

11: **end function**

1: **function** FIXHEADINGTRANSLATION$P_G(t_1, t_2)$

2:     filter intensity values for $\forall \vec{p}^*_G : p^*_{G_{int}} > \delta_{int}$

3:     form clusters $\mathcal{L}$ of line markings for P^*_G

4: establish correspondences for $\mathcal{L}(t_1)$ and $\mathcal{L}(t_2)$ and   compute R using (10) in the 2D case

5:     apply R and compute $\vec{t}$

6:     **return** $R_z(\phi), \vec{t}$

7: **end function**

$$\Delta\alpha = \arccos(n_z(t_{n-1})) - \arccos(n_z(t_n)),$$
$$\Delta o = (s_0(3), s_1(3), s_2(3))^T \left(C(t_{n-1}) \overline{C(t_n)} \right), \quad (11)$$

with $s_i(3)$ referring to the third element of the corresponding eigenvalues of the point subsets P_σ.

3.5.1 | Statistical testing

Within the scope of deformation monitoring, statistical tests objectively assess whether concrete panel's tilt and location (11) changed significantly. This essential aspect requires, however, knowledge about the variance of the key parameters (Caspary & Rüeger, 1987; Cooper, 1987). There exist two ways to derive statistical variance for each concrete panel.

1. **Error propagation.** The eigenvalues of the point cloud P_σ of a segmented concrete panel describe the data variance in direction of the principal components. Consequently, var $(\Delta o) = \lambda_3$. The uncertainty of the concrete panel orientation corresponds to the ratio of the eigenvalues of the covariance matrix var $(\beta_1, \beta_2) = [\lambda_3/\lambda_1, \lambda_3/\lambda_2]$ (Quinn & Ehlmann, 2019). var (β_1, β_2) describe the angular uncertainty in direction of the principal components $\vec{v}_1, \vec{v}_2$. According to its definition (8), DetMCD (deterministic algorithm for MCD) minimizes the product of the eigenvalues and not λ_3 solely. Thus, in most cases, λ_3 is smaller when using RANSAC. This fact is misleading, as it suggests RANSAC to yield more precise results, although $\Delta\alpha$ and Δo converge to the deterministic results of DetMCD when executed multiple times.

2. **Empirical quantities.** An alternative is to multiply sample each concrete panel and to compute the variance in tilt and location empirically. This solution is favorable, as it turns out that the theoretical quantities tend to overestimate the standard deviation by a factor of 5 to 15.

In terms of statistical testing, the null hypothesis becomes $H_0 : \mathbb{E}\{\Delta\alpha, \Delta o\} = 0$ and the alternative hypothesis is $H_a : \mathbb{E}\{\Delta\alpha, \Delta o\} \neq 0$. Given normally distributed populations with unknown but equal variances (derived empirically from one epoch), the test statistics for the mean differences $\hat{t} = (\Delta\hat{\alpha} - 0)/s_{\Delta\hat{\alpha}}$ follows a Student-t distribution. Consequently, we can derive thresholds for identifying significant deformations by rearranging the test criterion, that is, $|\Delta\hat{\alpha}| > s_{\Delta\hat{\alpha}} \cdot t_{f,0.975}$. Note that 95% is a standard value for the confidence interval in deformation monitoring (e.g., DIN 18710-1, 2010, p. 17).

4 | CASE STUDY

4.1 | Retaining structures

The retaining structures of this case study are located in the mountainous region of Bischofshofen in Salzburg, Austria. The selection includes five anchored walls along the motorways B311 and the A10 Tauern highway. Besides the fact that these objects have slender cross sections, a height up to 24 m while next to the highway and an age up to 50 years, inspections revealed anchor corrosion, which, in times of 24,000 vehicles closely passing by every day in 2019 on average, poses a high risk (Asfinag, 2020).

4.2 | Sensor hardware

Our methodology is not limited to a specific hardware or sensor manufacturer. Any MMS (laser scanners + positioning system) that is available for purchase on the market is applicable. In our project, the engineering company Amberg Technologies provided the MMS for the measurement campaigns. Besides two Z+F 9012 profile scanners (200 Hz mode), the MMS consists of a high-grade
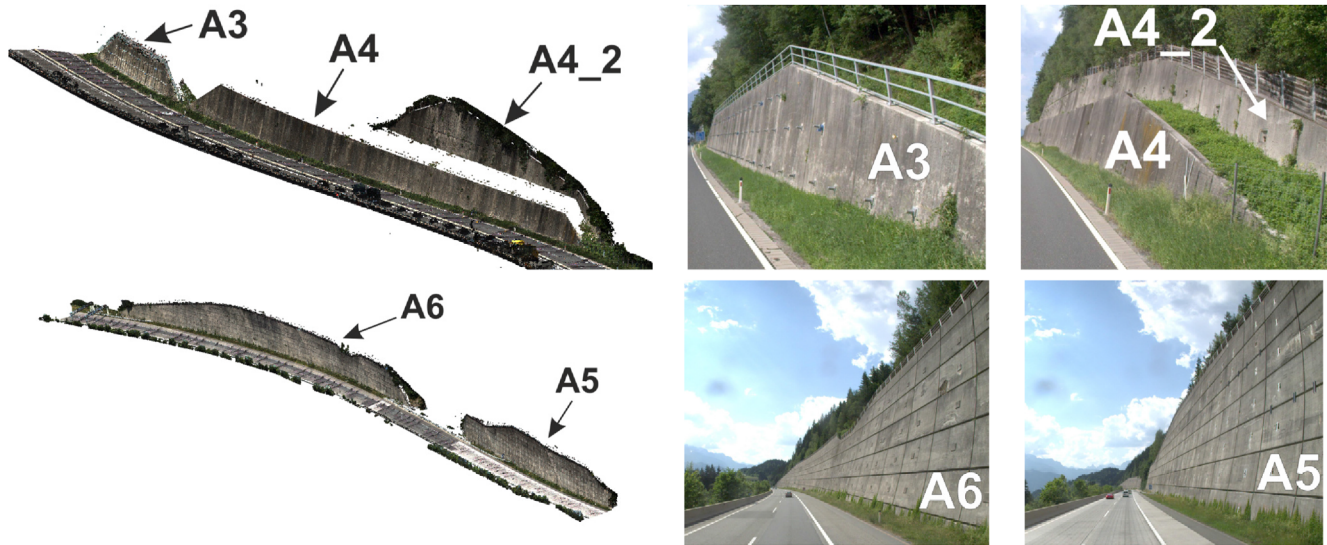
FIGURE 6 RGB colored point clouds (left) and detailed photos of the structures (right) of interest

TABLE 1 Information about selected retaining structures and the data acquisition

| ID | Height (m) | Length (m) | Observed in Epoch | | | |
			1	2	3	4
A3	6.5	85	X	X[a]	X	X
A4	6.5	255	X	X	X	X
A4_2	8	135		X	X	X
A5	22	400		X	X	X[a,b]
A6	23.5	370	X	X	X	X

Note: [a] New anchors installed before measurements.
[b] Wall refurbished; additional concrete elements installed.

TABLE 2 Dates and average temperatures at measurement campaigns

Epoch	Date	$\bar{T}$ (°C)
1	08-06-2016	22
2	20-06-2017	30
3	14-02-2018	−4
4	23-10-2018	13

positioning system: an Applanix LV510 positioning system (200 Hz) with a Trimble multi-GNSS, a fiber-optic-gyro IMU 46, and an odometer (distance measurement instrument [DMI]) attached to a rear wheel. In addition to the MMS' GNSS/IMU/DMI data, the computation of the trajectory incorporates GNSS data of surrounding control points of the Austrian reference network. The scanner's butterfly configuration is symmetrical, that is, ±45° w.r.t. driving direction and −30° w.r.t. the horizontal plane. This configuration is beneficial for minimizing shadowing while providing roughly the same distances and incidence angles for both scanners. The calibration of the lever arm took place shortly before the actual data acquisition.

4.3 | Data acquisition

Figure 6 gives an overview of the retaining structures, their relative location, and properties. For a better intuition about the dimensions, Table 1 points out their key parameters.

Structure A5 was not part of the measurement campaigns from the beginning and underwent a comprehensive refurbishment in 2018, leaving only two epochs available for deformation monitoring (see Table 1). Another aspect worth mentioning is that extensive vegetation at top of A4 shadowed the surface of A4_2 entirely in the first epoch (Table 1).

The ambient conditions differed significantly between the epochs (Table 2). While temperature is only one influencing factor, it deserves consideration when interpreting results (Section 5.3).

4.3.1 | Procedure

For the sake of comparability, the procedure of data collection was the same in all epochs. The MMS (installed on a car) was traveling on the first lane next to the emergency lane, while escort vehicles behind controlled the traffic for safety reasons. Each epoch, we passed by the structures five times to investigate varying driving speeds, ranging from 60 km/h (2×), 80 km/h (2×) to 100 km/h (1×).

TABLE 3 Parameter selection for individual processing steps

Parameter	Equation/Section	Description
$s_x = s_y = 0.15$ m	3.1	Grid cell size
$s_z = 1$ m	3.1	Grid cell height
$\delta_z = 0.01$ m	3.1	Ground removal criteria
$r_s = 0.25$, m	(6)	Small-scale radius
$r_s = 1.5$, m	(6)	Large-scale radius
$\|\Delta \vec{n}_{th}\| = 0.2$	(6)	DoN threshold
$c_d = 0.15$, m	3.2	Spatial clustering distance
$c_S = 10^4$	3.2	Spatial clustering size
$\Delta\alpha = 2.5°$	(9)	Enclosed angle of normals
$\Delta\Omega = 0.01$ m	(9)	Orthogonal distance
$\Delta\epsilon = 0.2$ m	(9)	Euclidean distance

TABLE 4 Absolute and relative execution times of the processing steps

Step	Abs. time (s)	Rel. time (%)
Ground extraction	2,447	25.3
Structure extraction	445	4.6
Robust normals	5,555	57.4
Panel segmentation	271	2.8
Panel modeling	27	0.3
Tilt compensation	911	9.4
Translation	16	0.2

4.4 | Data processing

Our processing methodology runs highly automated in C++ and Matlab. The implementations invoke PCL (Point Cloud Library v1.8.1, Rusu & Cousins, 2011) for point cloud processing, and the LIBRA library (Verboven & Hubert, 2005) for the robust MCD estimator.

Table 3 lists the parameters used for processing data of the case study. Most of them are robust regarding the parameter selection, while the homogeneity criteria for separating the concrete panels (9) are the most sensitive for the outcome. Depending on sensor noise or the type of wall, fine-tuning might be necessary.

The runtime that our implementation takes to output deformations from two point sets with approximately 25 million points each is around 2.5 h on a standard machine (i7 6800k, 64GB RAM). Table 4 indicates that those steps that involve the MCD estimator (e.g., robust normals) suffer from low efficiency, even when implemented in a parallelized fashion. The required runtime is an aspect to address in future. It is reducible by imple-

menting more intelligent pattern recognition methods. Nonetheless, the present implementation achieves a significant reduction of workload over conventional, manual approaches through automation.

5 | RESULTS

5.1 | Repeatability

Mobile mapping and tailored point cloud processing methods promise the delivery of valuable information for safety assessment along roads at high efficiency. However, the central question is whether we can trust this information.

For instance, if we pass by a retaining wall twice within a short time, does the proposed approach yield the same tilt α and location C for the concrete panels? What are the minimum tilt changes and deformations that can be detected?

Answers to these questions can give statistical analyses of our field studies. We can regard two tilt values α_1, α_2 of a segmented panel σ as statistically equal in case the hypothesis test fails to reject $H_0 : \mathbb{E}\{\alpha_2(\sigma) - \alpha_1(\sigma)\} = 0$.

The tilt difference distribution $\alpha_2 - \alpha_1$ (Figure 7) unveils interesting aspects for retaining walls A4 and A6 (samples of epoch 2017):

- The histograms approximate to normal distributions. The average panel tilt deviation centers around zero, hence $\mathbb{E}\{\alpha_2 - \alpha_1\} \approx 0$.
- The impact of the driving speed is negligible for our hardware setup (two laser scanners). There are no significant differences when driving 60, 80, or 100 km/h.
- In contrast, the panel height influences the variation of the values. This becomes obvious when comparing the distributions of A4 to A6. A4 consists of one row of panels with a height of 6.4 m. On the contrary, A6 is a structure with up to seven panels in a column, each of which with a height of 2.7 m.
- Based on the statistics, we derive the 95% confidence bounds for A3 and A4 to $c = \pm 0.03°$ ($\equiv \pm 3.5$ mm at 6.4 m height) and for A4_2, A5, and A6 to $c = \pm 0.05°$. These can serve as benchmark for identifying significant deformations.

The essence of our studies is that we can drive with up to 100 km/h and still achieve a remarkable repeatability of panel tilting with the described methodology. Converting panel tilting to the displacements at the top of a panel, we obtain ± 3.5 mm (95%), which compares to traditional surveying methods.

Within our considerations about the impact of driving speed, we assumed homogeneity across the structure.
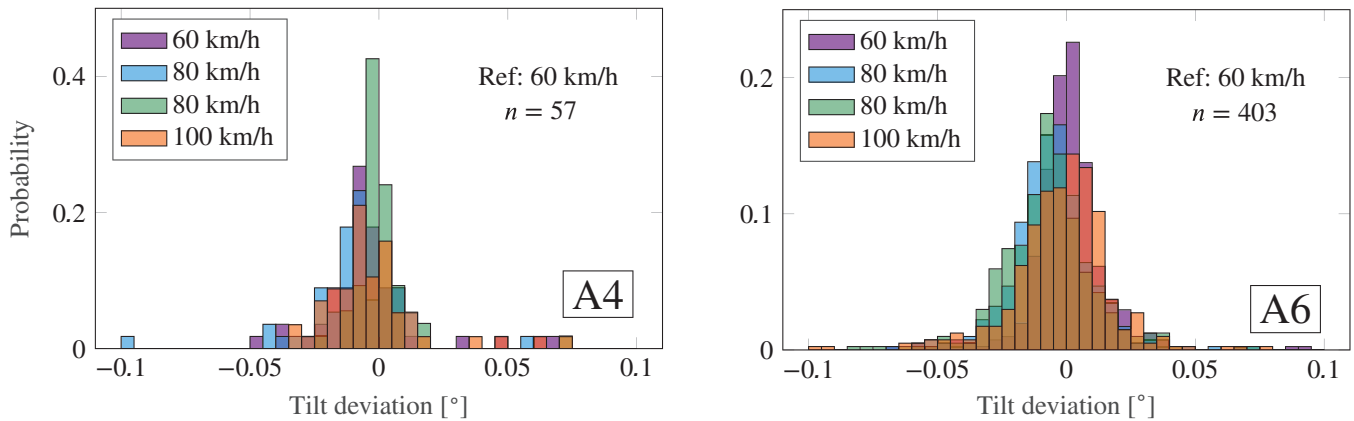
FIGURE 7 Histogram of panel tilt deviations for A4 (left) and A6 (right) w.r.t. reference drive (60 km/h)

Hence, instead of sampling each panel multiple times, we draw conclusions from all panels (sample size $n = 57/403$). While this works well for structures A5 and A6, it is less suitable for A3, A4, and A4_2 with a small number of concrete panels and with considerably varying heights (leading to outliers in Figure 7 , left). Our approach for A3 and A4 is hence to derive statistics for each panel separately. This time, the sample consists of the tilt values computed from each measurement drive (sample size $n = 5$).

5.1.1 | Lateral displacements

The same questions arise for relative panel displacements, as they turned out as indicators for the structural performance of high anchored retaining structures, for example, A5 and A6. Referring to the already described principle, we analyzed the reliability and obtained significance thresholds for lateral displacements of $c = \pm 1.5$ mm (95%) for A6 and A5 by taking all concrete panels into account. Individual panels reach deviations up to ± 3 mm.

5.2 | Systematic influences

Regarding the figures and numbers presented in Section 5.1, it is tempting to assume that mobile mapping could achieve superior repeatability to conventional surveying methods. The problem is that these values apply perfectly under constant conditions: sensor-to-object distance, environmental conditions, and hardware setup.

Figure 8 shows apparent tilt changes that resulted when collecting data of retaining structure A6 in two opposite driving directions. With the processing scheme presented in Section 3.4, we are able to compensate for calibration insufficiencies that evoke a horizon tilting of approximately 0.05° (shifting in the histogram).

5.3 | Deformations

5.3.1 | Structures A3 and A4

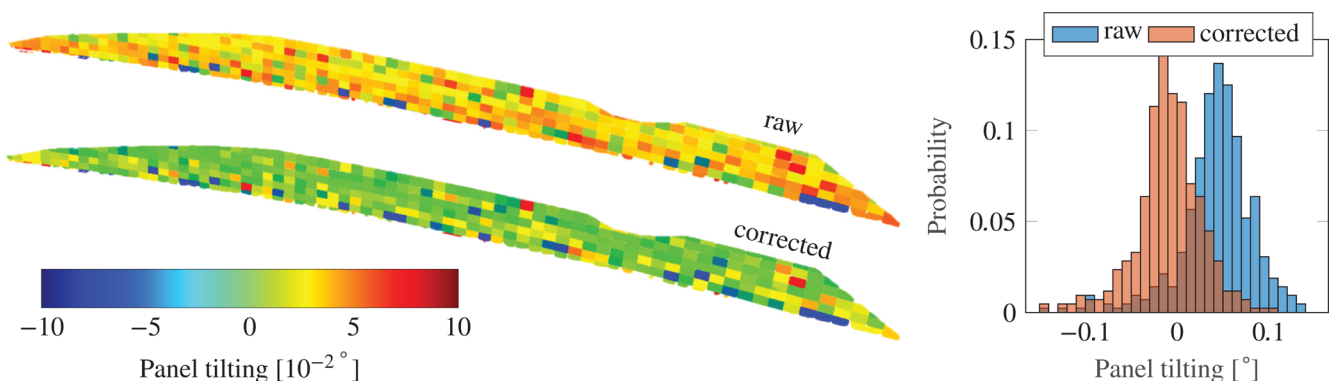We deployed our data processing strategy to the gathered data sets of all four epochs. Figure 9 depicts the computed

FIGURE 8 Panel tilting for data sets acquired in opposite driving directions: with and without compensation for systematic influences
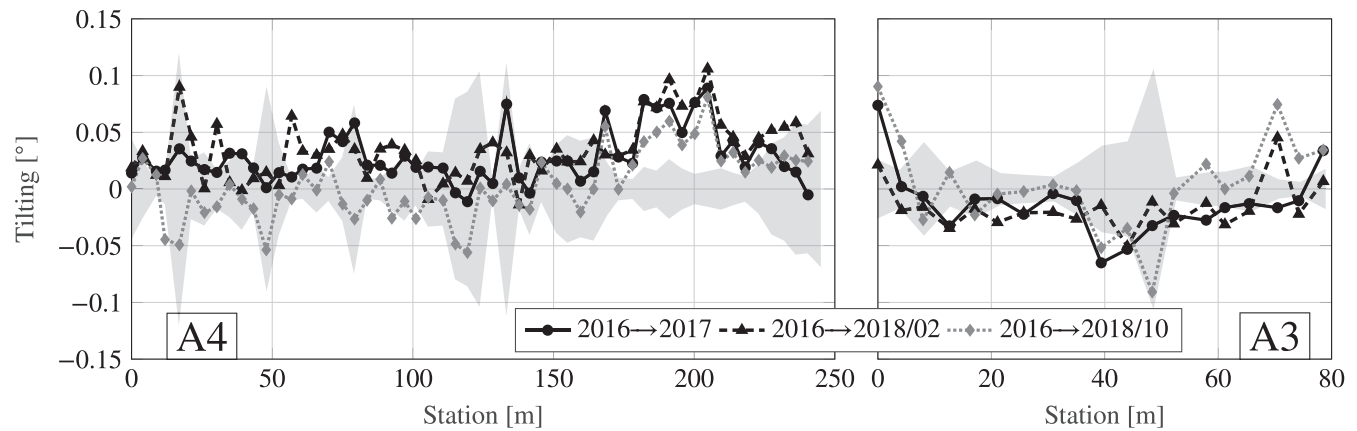
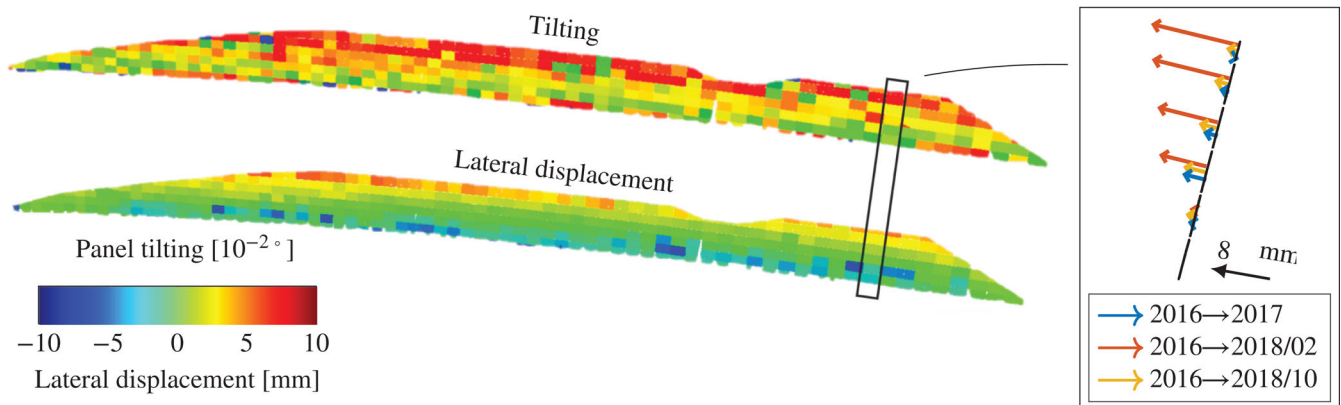**FIGURE 9** Panel tilting of individual concrete panels along structure for A4 (left) and A3 (right)

FIGURE 10 Deformations of A6 for epoch 1→3: panel tilting and lateral displacements (left) and multitemporal deformation of a cross section (gray rectangle) of A6: lateral displacements (right)

tilting for individual concrete panels alongside the structures A4 and A3. The reference epoch is 2016.

The gray bands indicate the thresholds for identifying significant deformations with 95% confidence. Regarding Figure 9, left, the majority of segmented concrete panels do not tilt significantly relative to epoch 2016. However, 10 consecutive of them (between station 170 and 220 m) consistently incline with a positive sign (toward the road) for all periods. Our modeling strategy highlights the good coincidence along the structure and across the epochs in this region, suggesting systematic changes but certainly no outliers. Nonetheless, even in the case of long-term deformations, there is no reason for concern, as the inclination stabilizes after epoch 2017.

In contrast, A3 (Figure 9, right) shows spikes at the boundaries (station <5 m and >70 m). It is worth mentioning that the size of these panels is small, and extensive vegetation covered the wall in 2016. Otherwise, deformation analysis approves the long-term stability of the structure, when regarding epoch 2017→2018/10. The reason for

the negative inclination changes (tilting toward the slope) might be the installation (and prestressing) of new anchors between epoch 2016 and 2017. Albeit significant tilting, structures deformed to no hazardous extent, though.

5.3.2 | Structures A5 and A6

The impact of seasonal variations (temperature and precipitation) on the high retaining structures A5 and A6 is considerable (Figure 10). At time of data collection, the air temperature difference between epoch 2016 and epoch 2018/02 was $\Delta T = -34$ K. As response to dramatically changing conditions, A6 showed significant tilting toward the highway in the upper part of up to +0.1° (threshold of ±0.05° derived in Section 5.1). This thermally induced impact leads to a banana-shape deformation pattern of A5 and A6. As a result, we see lateral displacements of the concrete panels on top of up to 12 mm (see Figure 10, right). This is a nonpermanent behavior of A6, as the structure relaxes in

the subsequent epoch. No significant deformations remain when comparing data of epochs 2016 and 2018/10.

5.3.3 | Validation

We use geodetic monitoring data for validating our results. An engineering company performed optical surveys to targets mounted on the anchored concrete panels. Based on the coordinate frame's orientation, we can directly compare our lateral displacement of A6 and A5 with the reference data (46 and 75 targets, respectively). For A3 and A4 (34 and 54 targets), we derive tilting from the coordinate differences of two targets aligned in a profile.

Reference data are available at infrequent intervals only, which, however, complies well with our results for A5 and A6 for the epochs 2016 to 2018/10. In fact, the reference measurements did not reveal any significant deformations for the structures. This holds true for structures A3 and A4 between 2017 and 2018/10 as well.

6 | CONCLUSION

Within this paper, we presented an approach for monitoring the tilt and the lateral displacement of a large number of retaining walls. An extensive field study revealed the method's high repeatability when using high-qualitative MMSs and our proposed processing pipeline. It exploits the high data redundancy and corrects for systematic influences that reached up to 0.05° in our case. The minimum tilt that is detectable is in the range of hundredths of a degree and for lateral displacements below ± 3.5 mm (with 95% confidence). These values compare to traditional surveying methods.

According to our evaluations, two of the investigated high retaining walls respond to seasonal variations and deform in the upper part with up to 12 mm. However, this is no lasting behavior, as no deformations remain when comparing the geometry under similar ambient conditions. Our results comply well with geodetic reference measurements, indicating no significant geometry changes by the end of the field study.

For infrastructure operators, the question is whether the structures behave as they expect them to. Structural monitoring can help, but it requires an accurate interpretation. Without numerical models or fundamental data, it is up to experts to distinguish between normal behavior and signs of deterioration. Most commonly, experts thus focus on identifying changes and anomalies.

The proposed method provides objective data for safety assessment while standing out in terms of efficiency. Its widespread application to many retaining walls at high fre-

quency (and different seasons) is promising for identifying abnormal behavior of objects at a large scale. Consequently, experts can then apply more detailed monitoring schemes to selected, critical structures.

REFERENCES
Admassu, K., Lynch, J., Athanasopoulos-Zekkos, A., & Zekkos, D. (2019). Long-term wireless monitoring solution for the risk management of highway retaining walls. In *SPIE: Nondestructive Characterization and Monitoring of Advanced Materials, Aerospace, Civil Infrastructure, and Transportation XIII*, Vol. *1097103* (p. 14).

Applanix. (2017). POS LV. February 2018.

Asfinag. (2020). Traffic census 2019. https://www.asfinag.at/verkehr/verkehrszaehlung/.

Barber, C. B., Dobkin, D. P., & Huhdanpaa, H. (1996). The Quickhull Algorithm for Convex Hulls. *ACM Transactions on Mathematical Software*, *22*, 469–483.

Blaskow, R., & Schneider, D. (2014). Analysis and correction of the dependency between laser scanner intensity values and range. In *International Archives of the Photogrammetry, Remote Sensing and Spatial Information Sciences - ISPRS Archives*.

Caspary, W., & Rüeger, J. (1987). *Concepts of network and deformation analysis*. Monograph. School of Surveying, University of New South Wales.

Cheng, L., Chen, S., Liu, X., Xu, H., Wu, Y., Li, M., & Chen, Y. (2018). Registration of laser scanning point clouds: A review. *Sensors*, *18*(1641), 25.

Choy, C., Park, J., & Koltun, V. (2019). Fully convolutional geometric features. In *International Conference on Computer Vision*, (p. 9), Seoul, Korea.

Cooper, M. (1987). *Control surveys in civil engineering*. New York: Nichols Publishing Company.

DIN 18710-1. (2010). *German standard: Engineering survey - part 1: General requirements* (Technical report). Berlin.

E. 1997-1. (2004). *Eurocode 7: Geotechnical design - Part 1: General rules.* (Technical report, Authority: The European Union Per Regulation 305/2011, Directive 98/34/EC, Directive 2004/18/EC). Brussels.

Ehrhart, M. (2017). *Applications of image-assisted total stations: Concepts, experiments, results and calibration* (Doctoral thesis). Graz University of Technology.

Eling, D. (2009). *Terrestrisches Laserscanning für die Bauwerksüberwachung*. (Deutsche Geodätische Kommission bei der Bayerischen Akademie der Wissenschaften/C: Dissertationen). Leibniz-Univ, Fachrichtung Geodäsie und Geoinformatik.

Friedli, E., Presl, R., & Wieser, A. (2019). Influence of atmospheric refraction on terrestrial laser scanning at long range. In V. Gikas (Ed.), *4th Joint International Symposium on Deformation Monitoring (JISDM)*, (p. 6), Athens, Greece.

Friedli, E., & Wieser, A. (2016). Identification of stable surfaces within point clouds for areal deformation monitoring. In *3rd Joint*

International Symposium on Deformation Monitoring (JISDM) in Vienna from 30th March-1st April.

Girardeau-Montaut, D., Roux, M., Marc, R., & Thibault, G. (2005). Change detection on points cloud data acquired with a ground laser scanner. In *International Archives of the Photogrammetry, Remote Sensing and Spatial Information Sciences - ISPRS Archives*.

Gojcic, Z., Zhou, C., & Wieser, A. (2019). Robust point correspondences for point cloud based deformation monitoring of natural structures. In V. Gikas (Ed.), *4th Joint International Symposium on Deformation Monitoring* (p. 8). Athens, Greece: National Technical University of Athens.

Gordon, S. J., & Lichti, D. (2007). Modeling terrestrial laser scanner data for precise structural deformation measurement. *Journal of Surveying Engineering*, *133*, 72–80.

Guo, Y., Bennamoun, M., Sohel, F., Lu, M., Wan, J., & Kwok, N. M. (2016). A comprehensive performance evaluation of 3D local feature descriptors. *International Journal of Computer Vision*, *116*, 66–89.

Hackel, T., Wegner, J. D., & Schindler, K. (2016). Fast semantic segmentation of 3D point clouds with strongly varying density. *ISPRS Annals of the Photogrammetry, Remote Sensing and Spatial Information Sciences*, *3*, 177–184.

Heinz, E., Eling, C., Klingbeil, L., & Kuhlmann, H. (2019). Monitoring the planarity and subsidence of a motorway using kinematic laser scanning. In V. Gikas (Ed.), *Proceedings of the 4th Joint International Symposium on Deformation Monitoring (JISDM)*, (p. 8), Athens, Greece.

Holst, C., Neuner, H., Wieser, A., Wunderlich, T., & Kuhlmann, H. (2016). Calibration of terrestrial laser scanners. *AVN Allgemeine Vermessungsnachrichten*, *123*(5), 147–157.

Holst, C., Nothnagel, A., Blome, M., Becker, P., Eichborn, M., & Kuhlmann, H. (2015). Improved area-based deformation analysis of a radio telescope's main reflector based on terrestrial laser scanning. *Journal of Applied Geodesy*, *9*, 1–13.

Holst, C., Schmitz, B., Schraven, A., & Kuhlmann, H. (2017). Eignen sich in Standardsoftware implementierte Punktwolkenvergleiche zur flächenhaften Deformationsanalyse von Bauwerken?: Eine Fallstudie anhand von Laserscans einer Holzplatte und einer Staumauer. *ZFV - Zeitschrift fur Geodasie, Geoinformation und Landmanagement*, *142*(2), 98–110.

Horn, B. K. (1984). Extended Gaussian images. *Proceedings of the IEEE*, *72*, 1671–1686.

Hubert, M., Debruyne, M., & Rousseeuw, P. J. (2018). Minimum covariance determinant and extensions. *Wiley Interdisciplinary Reviews: Computational Statistics*, *10*(3), e1421.

Ioannou, Y., Taati, B., Harrap, R., & Greenspan, M. (2012). *Difference of normals as a multi-scale operator in unorganized point clouds*. Second International Conference on 3D Imaging, Modeling, Processing, Visualization & Transmission, Zurich (pp. 501–508).

Jaakkola, A., Hyyppä, J., Hyyppä, H., & Kukko, A. (2008). Retrieval algorithms for road surface modelling using laser-based mobile mapping. *Sensors*, *8*, 5238–5249.

Javanmardi, E., Javanmardi, M., Gu, Y., & Kamijo, S. (2018). Autonomous vehicle self-localization based on probabilistic planar surface map and multi-channel LiDAR in urban area. In *IEEE Conference on Intelligent Transportation Systems, Proceedings, ITSC*.

Kregar, K., Ambrožiĉ, T., Kogoj, D., Vezoĉnik, R., & Marjetiĉ, A. (2015). Determining the inclination of tall chimneys using the TPS

and TLS approach. *Measurement: Journal of the International Measurement Confederation*, *75*, 354–363.

Ladstädter, R., Luley, P., Ladstätter, S., & Mayer, H. (2019). UHD Mapping von Teststrecken für automatisiertes Fahren. In T. P. Kersten (Ed.), *Dreiländertagung der DGPF, der OVG und der SGPF*, (pp. 175–187), Vienna, Austria. Deutsche Gesellschaft für Photogrammetrie, Fernerkundung und Geoinformation.

Laefer, D., & Lennon, D. (2008). Viability assessment of terrestrial LiDAR for retaining wall monitoring. In *Geotechnical special publication*. Reston, VA: American Society of Civil Engineers.

Lague, D., Brodu, N., & Leroux, J. (2013). Accurate 3D comparison of complex topography with terrestrial laser scanner: Application to the Rangitikei Canyon (N-Z). *ISPRS Journal of Photogrammetry and Remote Sensing*, *82*, 10–26.

Lienhart, W. (2017). Geotechnical monitoring using total stations and laser scanners: Critical aspects and solutions. *Journal of Civil Structural Health Monitoring*, *7*, 315–324.

Lin, Y.-J., Habib, A., Bullock, D., & Prezzi, M. (2019). Application of high-resolution terrestrial laser scanning to monitor the performance of mechanically stabilized earth walls with precast concrete panels. *Journal of Performance of Constructed Facilities*, *33*(5), 04019054.

Ma, L., Li, Y., Li, J., Wang, C., Wang, R., & Chapman, M. A. (2018). Mobile laser scanned point-clouds for road object detection and extraction: A review. *Remote Sensing*, *10*, 1531.

McGuire, M. P., Yust, M. B. S., & Collin, J. G. (2016). As-built verification, condition assessment, and forensic analysis of mechanically-stabilized earth walls incorporating terrestrial lidar. *Geotechnical and Structural Engineering Congress*, (pp. 467–482).

Mikrut, S., Kohut, P., Pyka, K., Tokarczyk, R., Barszcz, T., & Uhl, T. (2016). Mobile laser scanning systems for measuring the clearance gauge of railways: State of play, testing and outlook. *Sensors (Switzerland)*, *16*.

Mukupa, W., Roberts, G. W., Hancock, C. M., & Al-Manasir, K. (2017). A review of the use of terrestrial laser scanning application for change detection and deformation monitoring of structures. *Survey Review*, *49*, 99–116.

Nurunnabi, A., Belton, D., & West, G. (2014). Robust statistical approaches for local planar surface fitting in 3D laser scanning data. *ISPRS Journal of Photogrammetry and Remote Sensing*, *96*, 106–122.

Oats, R., Escobar-Wolf, R., & Oommen, T. (2017). A novel application of photogrammetry for retaining wall assessment. *Infrastructures*, *2*(3), 10.

Oskouie, P., Becerik-Gerber, B., & Soibelman, L. (2016). Automated measurement of highway retaining wall displacements using terrestrial laser scanners. *Automation in Construction*, *65*, 86–101.

Park, H. S., Lee, H. M., Adeli, H., & Lee, I. (2007). A new approach for health monitoring of structures: Terrestrial laser scanning. *Computer-Aided Civil and Infrastructure Engineering*, *19*, 19–30.

Park, S., Park, H., Kim, J., & Adeli, H. (2015). 3D displacement measurement model for health monitoring of structures using a motion capture system. *Measurement*, *59*, 352–362.

Pauly, M., Gross, M., & Kobbelt, L. P. (2002). Efficient simplification of point-sampled surfaces. In *Proceedings of the IEEE Visualization Conference*.

Quinn, D. P., & Ehlmann, B. L. (2019). A PCA-based framework for determining remotely sensed geological surface orientations

and their statistical quality. *Earth and Space Science*, *6*, 1378–1408.

Rebhan, M. J., Marte, R., Tschuchnigg, F., Vorwagner, A., & Kwapisz, M. (2019). Safety assessment of existing retaining structures. In H. Sigursteinsson (Ed.), *The XVII European Conference on Soil Mechanics and Geotechnical Engineering*, (p. 8), Reykjavik, Iceland. Icelandic Geotechnical Society.

Rebhan, M. J., Marte, R., Vorwagner, A., Tschuchnigg, F., & Kwapisz, M. (2019). Corrosion damage to cantilever MR walls - Representation in tests and calculations. *Geomechanics and Tunnelling*, *12*(5), 506–514.

Rousseeuw, P. J., & Driessen, K. V. (1999). A fast algorithm for the minimum covariance determinant estimator. *Technometrics*, *41*(3), 212–223.

Rusu, R. B., & Cousins, S. (2011). 3D is here: Point Cloud Library (PCL). In *2011 IEEE International Conference on Robotics and Automation*, (pp. 1–4).

Saarenketo, T., & Silvast, M. (2019). Using laser scanner and GPR data in geotechnical diagnostics of roads and railways. In *European Conference on Soil Mechanics and Geotechnical Engineering*, (p. 8), Reykjavik Iceland.

Schmitt, C., Kromoser, B., Harmening, C., Falkner, J., Neuner, H.-B., & Kollegger, J. (2017). Geodetic surface based methods for applications in civil engineering. In A. Kopáčik et al. (Eds.), *Ingeo 2017: Proceedings of the 7th International Conference on Engineering Surveying, Invited; talk: 7th International Conference on Engineering Surveying, Lisbon, October 18–20, 2017 (pp. 275–284)*.

Schneider, O., Prokopová, A., Modetta, F., & Petschen, V. (2019). The use of artificial intelligence for a cost-effective tunnel maintenance. In *Tunnels and Underground Cities: Engineering and Innovation Meet Archaeology, Architecture and Art - Proceedings of the WTC 2019 ITA-AITES World Tunnel Congress*.

Serantoni, E., & Wieser, A. (2016). TLS-based deformation monitoring of snow structures. In C. Holst (Ed.), *Terrestrisches Laserscanning 2016 (TLS 2016), Vol. 85 of Schriftenreihe des DVW*, (pp. 89–102). Augsburg: Wissner-Verlag.

Sesselmann, M., Stricker, R., & Eisenbach, M. (2019). Einsatz von Deep Learning zur automatischen Detektion und Klassifikation von Fahrbahnschäden aus mobilen LiDAR-Daten. *AGIT - Journal für Angewandte Geoinformatik*, *5*, 100–114.

Sharma, S., Prabhu, N. V., Naveen, Y., & Bhuvaneshwari, S. (2020). Numerical modelling of lateral deformation of the cantilever retaining wall in expansive clays. In S. Saride, B. Umashankar, & D. Avirneni (Eds.), *Advances in geotechnical and transportation engineering* (pp. 233–247). Singapore: Springer Singapore.

Sorkine, O. (2009). Least-squares rigid motion using svd. *Technical notes*, *120*(3), 52. https://scholar.google.ch/scholar?oi=bibs&hl=en&cluster=5197490735998670007

Soudarissanane, S., Lindenbergh, R., Menenti, M., & Teunissen, P. (2011). Scanning geometry: Influencing factor on the quality of terrestrial laser scanning points. *ISPRS Journal of Photogrammetry and Remote Sensing*, *66*, 389–399.

Spezialetti, R., Salti, S., & Di Stefano, L. (2019). Performance evaluation of learned 3D features. In E. Ricci, S. Rota Bulò, C. Snoek, O. Lanz, S. Messelodi, & N. Sebe (Eds.), *Image Analysis and Processing – ICIAP 2019* (pp. 519–531). Cham: Springer International Publishing.

Tapken, P. (2018). Mobile mapping trends and insights. *GIM International*, *32*(4), 22–25.

Tombari, F., Salti, S., & Di Stefano, L. (2013). Performance evaluation of 3D keypoint detectors. *International Journal of Computer Vision*, *102*, 198–220.

Tsin, Y., & Kanade, T. (2004). A correlation-based approach to robust point set registration. In T. Pajdla & J. Matas (Eds.), *Computer Vision-ECCV 2004* (pp. 558–569). Berlin, New York: Springer Berlin Heidelberg.

Tung, S. H., Weng, M. C., & Shih, M. H. (2013). Measuring the in situ deformation of retaining walls by the digital image correlation method. *Engineering Geology*, *166*, 116–126.

Verboven, S., & Hubert, M. (2005). LIBRA: A MATLAB library for robust analysis. *Chemometrics and Intelligent Laboratory Systems*, *75*, 127–136.

Vosselman, G., & Maas, H.G. (Eds.) (2010). *Airborne and terrestrial laser scanning*. Boca Raton, FL: CRC Press. https://research.utwente.nl/en/publications/airborne-and-terrestrial-laser-scanning-2.

Wujanz, D., Burger, M., Mettenleiter, M., & Neitzel, F. (2017). An intensity-based stochastic model for terrestrial laser scanners. *ISPRS Journal of Photogrammetry and Remote Sensing*, *125*, 146–155.

Yoo, C., & Lee, K. M. (2003). Instrumentation of anchored segmental retaining wall. *Geotechnical Testing Journal*, *26*(4), 382–389.

How to cite this article: Kalenjuk S, Lienhart W, Rebhan MJ. Processing of mobile laser scanning data for large-scale deformation monitoring of anchored retaining structures along highways. *Comput Aided Civ Inf*. 2021;*36*:678–694. https://doi.org/10.1111/mice.12656